

Controlling Phase Assemblage in a Complex Multi-Cation System: Phase-Pure Room Temperature Multiferroic $(1-x)\text{BiTi}_{(1-y)/2}\text{Fe}_y\text{Mg}_{(1-y)/2}\text{O}_{3-x}\text{CaTiO}_3$

Pranab Mandal, Michael J. Pitcher, Jonathan Alaria, Hongjun Niu, Marco Zanella, John B. Claridge,* and Matthew J. Rosseinsky*

A room temperature magnetoelectric multiferroic is of interest as, e.g., magnetoelectric random access memory. Bulk samples of the perovskite $(1-x)\text{BiTi}_{(1-y)/2}\text{Fe}_y\text{Mg}_{(1-y)/2}\text{O}_{3-x}\text{CaTiO}_3$ (BTFM-CTO) are simultaneously ferroelectric, weakly ferromagnetic, and magnetoelectric at room temperature. In BTFM-CTO, the volatility of bismuth oxide, and the complex subsolidus reaction kinetics, cause the formation of a microscopic amount of ferrimagnetic spinel impurity, which complicates the quantitative characterization of their intrinsic magnetic and magnetoelectric properties. Here, a controlled synthesis route to single-phase bulk samples of BTFM-CTO is devised and their intrinsic properties are determined. For example, the composition $x = 0.15$, $y = 0.75$ shows a saturated magnetization of $0.0097\mu_B$ per Fe, a linear magnetoelectric susceptibility of $0.19(1) \text{ ps m}^{-1}$, and a polarization of $66 \mu\text{C cm}^{-2}$ at room temperature. The onset of weak ferromagnetism and linear magnetoelectric coupling are shown to coincide with the onset of bulk long-range magnetic order by neutron diffraction. The synthesis strategy developed here will be invaluable as the phase diagram of BTFM-CTO is explored further, and as an example for the synthesis of other compositionally complex BiFeO_3 -related materials.

1. Introduction

A multiferroic material^[1] combines ferroelectricity and ferromagnetism in the same phase. The synthesis of a bulk material where both types of long-range order are present at room temperature is challenging because the electronic structure requirements of these two states are different and in competition with each other. A strong magnetoelectric coupling^[2] between the

order parameters would lead to switching of the electrical polarization (P) by the magnetic field H , or the magnetization (M) by the electric field E , which has been proposed as a possible candidate to replace the presently used volatile random access memories (RAM).^[3,4] A magnetoelectric multiferroic memory would benefit from nonvolatility and nondestructive reading of magnetic RAM and the low-power, high-speed features of ferroelectric RAM.^[3,4] Bulk BiFeO_3 exhibits both ferroelectric and long-range magnetic order at room temperature, however it is a pure antiferromagnet because the cycloidal magnetic ordering leads to cancellation of the Dzyaloshinsky–Moriya interaction-mediated canted moments, and also prevents any linear magnetoelectric effect.^[5–8] The cycloidal ordering can be destabilized in strained and nanostructured films of BiFeO_3 leading to finite magnetization.^[9,10] Electric field-induced switching of the magnetization of a ferromagnetic

layer coupled to BiFeO_3 has been demonstrated in thin film devices.^[10,11] Powder neutron diffraction (PND) and Mössbauer studies show that $\text{PbFe}_{0.5}\text{Ta}_{0.5}\text{O}_3$, $\text{PbFe}_{0.5}\text{Ta}_{0.5}\text{O}_3\text{–PbTiO}_3$ solid solution, and the Aurivillius phases $\text{Bi}_{n+1}\text{Fe}_{n-3}\text{Ti}_3\text{O}_{3n+3}$ ($3.5 \leq n \leq 7$) are not long-range magnetically ordered at room temperature.^[12–15] field-induced switching of ferroelectric domains has been demonstrated in lamellae of $[\text{Pb}(\text{Zr}_{0.53}\text{Ti}_{0.47})\text{O}_3]_{0.6}\text{–}[\text{Pb}(\text{Fe}_{0.5}\text{Ta}_{0.5})\text{O}_3]_{0.4}$ and thin film $\text{Bi}_6\text{Ti}_{2.8}\text{Fe}_{1.52}\text{Mn}_{0.68}\text{O}_{18}$ ($n = 5$) at room temperature.^[16,17] Recently, we have reported a generic design route for room temperature multiferroic materials that integrates a percolating network of magnetic ions to produce long-range magnetic order with enhanced ferroelectric switching properties at the morphotropic phase boundary (MPB) between two polar phases with different polarization directions. This was exemplified in the perovskite oxide $(1-x)\text{BiTi}_{(1-y)/2}\text{Fe}_y\text{Mg}_{(1-y)/2}\text{O}_{3-x}\text{CaTiO}_3$ (BTFM-CTO) system, using techniques that definitively proved the coexistence and switchability of both orders within the perovskite structure.^[18] The order parameters are not only switchable at room temperature but are also coupled as demonstrated by the linear magnetoelectric effect.^[18] The structure of the perovskite at the MPB is complex and has been the subject of detailed studies over

Dr. P. Mandal, Dr. M. J. Pitcher, Dr. H. Niu,
Dr. M. Zanella, Dr. J. B. Claridge, Prof. M. J. Rosseinsky
Department of Chemistry
University of Liverpool
Liverpool L69 7ZD, UK
E-mail: j.b.claridge@liv.ac.uk; m.j.rosseinsky@liv.ac.uk



Dr. J. Alaria
Department of Physics
University of Liverpool
Liverpool L69 7ZE, UK

This is an open access article under the terms of the Creative Commons Attribution License, which permits use, distribution and reproduction in any medium, provided the original work is properly cited.

DOI: 10.1002/adfm.201504911

many years (notably for $\text{PbZr}_{1-x}\text{Ti}_x\text{O}_3$).^[19,20] Powder X-ray diffraction (PXRD) patterns of BTFM–CTO compositions at the MPB can be fitted to a two phase model with rhombohedral ($R3c$) and orthorhombic ($Pna2_1$) unit cells, or to a single monoclinic unit cell in space group $P11a$ (which is a sub group of $R3c$ and $Pna2_1$) using the Le Bail method.^[18] The compositions with $\gamma \geq 0.60$ reported so far contain small amounts of ferrimagnetic spinel impurities, which complicate the quantitative characterization of their intrinsic magnetic and magnetoelectric properties. Such impurities commonly form as kinetic products in systems with a mixture of refractory and volatile starting reagents, as the high temperatures required to drive the reaction to completion also promote the evaporation of the volatile component (e.g., phase-pure $\text{PbMg}_{1/3}\text{Nb}_{2/3}\text{O}_3$ (PMN) is difficult to synthesize from refractory MgO , Nb_2O_5 , and volatile PbO due to the formation of Pb-deficient pyrochlore impurities).^[21] Such secondary phases are common in BiFeO_3 -related compounds and are often difficult to eliminate.^[22–24]

The synthesis and processing of single-phase samples of the ternary oxide BiFeO_3 is complicated by the ready formation of sillenite ($\text{Bi}_{25}\text{FeO}_{39}$)-type and mullite ($\text{Bi}_2\text{Fe}_4\text{O}_9$)-type secondary phases^[25–27] which exist in thermodynamic equilibrium with BiFeO_3 between 720 and 1040 K,^[28] and whose stability is increased by the presence of trace impurities in the starting materials Bi_2O_3 and Fe_2O_3 .^[25] Attempts to avoid the formation of these phases by sintering at a higher temperature of 1098 K (above the melting point of Bi_2O_3) can lead to volatilization of bismuth, which promotes the formation of the Fe-rich mullite phase.^[25] Phase-pure BiFeO_3 can be prepared when the reaction conditions are suitably controlled, e.g., by using ultrapure (99.9995%) starting materials reacted at 1073 K under sacrificial powder to prevent bismuth loss.^[25] The sillenite and mullite phases do not generate strong features in $M(H)$ experiments as they are paramagnetic at room temperature,^[29–31] but strongly magnetic impurities have been shown to form in more complex phase fields (e.g., garnet-type $\text{R}_3\text{Fe}_5\text{O}_{12}$ impurities in quaternary lanthanide-doped $\text{Bi}_{1-x}\text{R}_x\text{FeO}_3$ derivatives)^[24] or under different reaction conditions (e.g., spinel-type Fe_3O_4 impurities in nanocrystalline BiFeO_3).^[22] These secondary phases, which may be present in amounts close to or below the sensitivity limits of X-ray diffraction, are undesirable as they make the observed magnetic properties difficult to interpret correctly.

The synthesis of phase-pure BiFeO_3 is challenging, but BTFM–CTO has a more complex composition (it contains five different cations versus two for BiFeO_3) offering many more potential kinetic pathways to formation and decomposition that are not available to BiFeO_3 . It also contains a combination of refractory and volatile components: a hydrated magnesium carbonate hydroxide is used in place of MgO as a reactive source of Mg during the synthesis of BTFM–CTO to minimize problems with slow reaction kinetics, but the formation of refractory MgFe_2O_4 as an intermediate phase simply reintroduces this problem in situ. Once formed, the complete consumption of MgFe_2O_4 requires a stoichiometric quantity of a reactive Bi source, a sufficiently high temperature to overcome the slow kinetics and sufficient heating time; the absence of any one of these factors (e.g., by evaporation of Bi_2O_3) would result in residual amounts of MgFe_2O_4 in the product.

This makes the synthesis of phase-pure BTFM–CTO challenging, although does not impede the use of methods such as Mössbauer spectroscopy that directly probe magnetic order at each iron nucleus to demonstrate the long-range magnetic order at room temperature in the multiferroic compositions. We report the development of a synthetic route that affords spinel-free multiferroic BTFM–CTO compositions, and measure their intrinsic magnetic, magnetoelectric, and ferroelectric properties.

2. Results and Discussion

2.1. Identification of the Spinel Impurity in BTFM–CTO and Its Contribution to Magnetism

Seven compositions in the range $x = 0.15$, $0.60 \leq \gamma \leq 0.90$ were prepared by the previously reported synthesis protocol.^[18] DC and AC magnetization measurements on $x = 0.15$, $\gamma = 0.80$ in the temperature range 10–650 K show only two magnetic ordering transitions at $T_N = 367$ K and $T_{N2} = 586$ K (Figure 1c; Figure S2a, Supporting Information) and none below room temperature; Mössbauer spectroscopy previously demonstrated that the perovskite phase is magnetically ordered at 300 K and this ordering accounts for the transition at T_N ,^[18] whereas T_{N2} matches closely to a nanocrystalline MgFe_2O_4 spinel phase,^[32] whose presence is confirmed by PXRD after a sufficiently long data collection time (Figure 1a). The sample exhibits constricted $M(H)$ loops below T_N and superparamagnetic-like $M(H)$ loops above T_N (Figure 1d) consistent with the presence of a small amount (≈ 0.7 wt% for $x = 0.15$, $\gamma = 0.80$) of ferrimagnetic spinel phase. Above T_{N2} , $M(H)$ isotherms are linear (Figure S2c, Supporting Information), showing that the only two magnetic phases present are the spinel impurity and the bulk perovskite. These features are common to all of the measured spinel-containing compositions, whose Néel temperatures (T_N) are tunable between 205 K and 441 K (Figure S1, Supporting Information). PND, which provides a crystallographic probe of long-range magnetic order that is sensitive to the different phases present, was employed to verify the Néel temperature of the perovskite for two different spinel-containing compositions: $x = 0.15$, $\gamma = 0.60$ and 0.80 . The 300 K PND pattern shows an intense reflection at 4.57 \AA (Figure 1b) that is not present in the PXRD pattern, which is characteristic of G-type antiferromagnetic ordering in perovskite orthoferrites,^[33] and is consistent with the 300 K Mössbauer spectra.^[18] The disappearance of this magnetic Bragg peak on warming occurs simultaneously with a sharp decrease in magnetization (T_N) in both of the samples that were measured ($x = 0.15$, $\gamma = 0.80$ as shown in Figure 1c; $x = 0.15$, $\gamma = 0.60$ as shown in Figure S3 in the Supporting Information), which provides additional confirmation that this component of the magnetization arises from intrinsic weak ferromagnetism in the perovskite and is consistent with the onset of a large linear magnetoelectric effect at T_N .^[18]

2.2. Synthesis of Single-Phase (Spinel-Free) BTFM–CTO

The complete scheme for the optimization of the synthetic procedure, described below, is illustrated in Figure S4 and full descriptions of all synthetic procedures are given in the

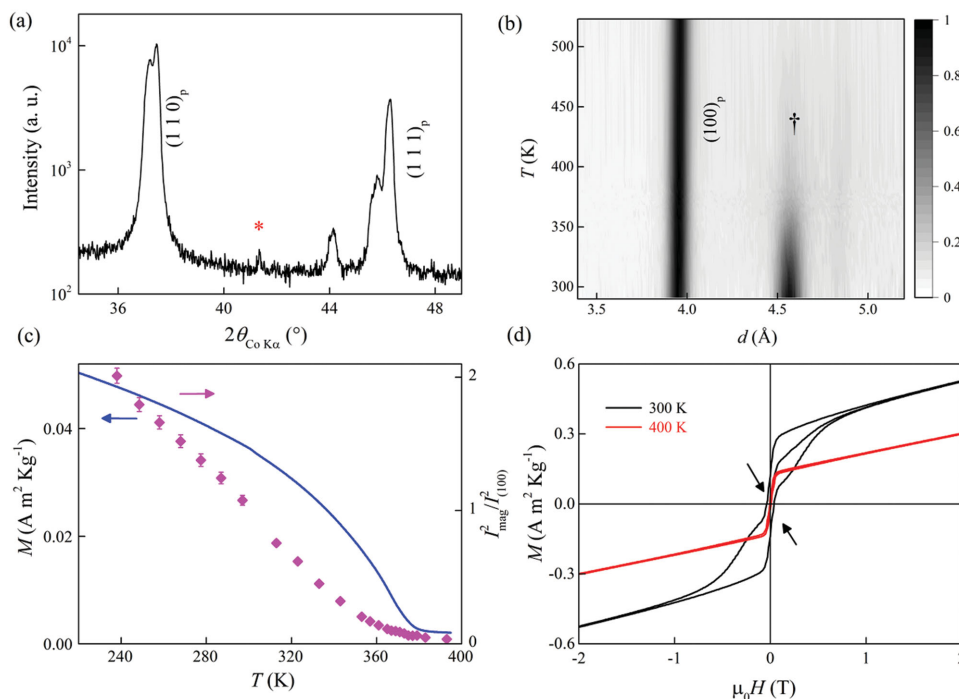


Figure 1. Magnetic properties of spinel-containing samples of $0.85\text{BiTi}_{0.10}\text{Fe}_{0.80}\text{Mg}_{0.10}\text{O}_3\text{--}0.15\text{CaTiO}_3$ ($x = 0.15$, $\gamma = 0.80$). a) Selected region of a laboratory PXRD pattern, collected for 8 h over the range $5^\circ \leq 2\theta \leq 130^\circ$, with intensity plotted on a logarithmic scale to emphasize the strongest peak of the cubic spinel impurity (asterisk). b) Temperature evolution of the nuclear $(100)_p$ Bragg peak and the most intense magnetic Bragg peak (\dagger) from 20 PND patterns in the range 290–525 K (Polaris bank 2, $2\theta = 26.5^\circ$). The dominant magnetic Bragg peak at ≈ 4.5 Å is characteristic of G-type antiferromagnetic ordering in a perovskite. c) Temperature dependence of thermal remanent magnetization (left axis, blue line) and ratio of the squared magnetic and $(100)_p$ nuclear Bragg peak intensities ($I_{\text{mag}}^2/I_{100}^2$) from PND (right axis, filled purple diamonds), showing that the onset of magnetization is coincident with long-range magnetic ordering. Error bars represent one standard deviation. d) Magnetic isotherms at 300 K (black, $T < T_N$) and 400 K (red, $T > T_N$). The constriction in the 300 K $M(H)$ marked by the arrows and the superparamagnetic-like feature in the 400 K $M(H)$ isotherm are consistent with the presence of the spinel-type magnetic impurity phase.

Supporting Information. A shortened version of the previously reported synthetic protocol for $x = 0.15$, $\gamma = 0.80$ ^[18] was taken as a starting point, which we refer to as Protocol 1. This protocol was then improved systematically until the ferrimagnetic spinel phase was eliminated. The effectiveness of each successive protocol in reducing the ferrimagnetic MgFe_2O_4 impurity was evaluated qualitatively from the shape of their magnetization isotherms (Figure S8, Supporting Information) and quantitatively from the extracted remanent magnetization values (M_r) at 395 K (i.e., above T_N for the perovskite but below T_{N2} for the spinel), which are tabulated in Table S1 (Supporting Information). Protocol 1 produced a sample with remanent magnetization of $0.0971 \text{ A m}^2 \text{ kg}^{-1}$ at 395 K. The first three iterations (Protocols 2–4) involved replacement of the starting reagent $\text{MgCO}_3\cdot\text{Mg}(\text{OH})_2\cdot 3\text{H}_2\text{O}$ (Alfa Aesar, 99.996%) with $(\text{MgCO}_3)_4\cdot\text{Mg}(\text{OH})_2\cdot 5\text{H}_2\text{O}$ (Sigma Aldrich, 99.99%); the packing of the reaction pellet in a 10-fold excess of sacrificial powder during sintering to minimize the volatilization of Bi_2O_3 ; and the introduction of an extra heating cycle prior to pelletizing to react the hydroxide and carbonate precursors at moderate temperatures prior to the final sintering. Together this produced a sample with a remanent magnetization of $0.0190 \text{ A m}^2 \text{ kg}^{-1}$. Further reduction of the remanent magnetization was gained after Protocols 5 and 6: this involved replacement of the original Bi_2O_3 starting reagent (Alfa Aesar, 99.99%)

by an ultrapure Bi_2O_3 reagent (Alfa Aesar, 99.9995%), followed by replacement of the hand grinding step by a second ball milling step (producing $M_r = 0.0112 \text{ A m}^2 \text{ kg}^{-1}$). By this point the magnetic spinel impurity content is reduced drastically: its presence is evident only from a small opening of the $M(H)$ loop at 395 K (Figure S8f, Supporting Information).

To understand the phase evolution as the reaction proceeds, PXRD patterns were collected from each of the intermediate steps of Protocol 6 (Figure S6, Supporting Information). During the three-step heating cycle, sillenite ($\text{Bi}_{25}\text{FeO}_{39}$) becomes the first major phase to form at 833 K, with the perovskite then forming the dominant phase at 1023 K with sillenite, $\text{Bi}_{1.6}\text{Ca}_{0.4}\text{O}_{2.8}$, $\text{Bi}_5\text{FeTi}_3\text{O}_{15}$, and MgFe_2O_4 spinel present as minor components. After the final firing at 1213 K, the sample appears to be a phase-pure perovskite by PXRD but retains a trace amount of magnetic spinel (Figure S8f, Supporting Information). Hence Protocol 6 contains only one milling and firing step between the first appearance of MgFe_2O_4 and arrival at the final product, which is insufficient to remove this phase entirely.

This was addressed in the final protocol (Protocol 7) by using thermogravimetric analysis (TGA)-optimized temperatures (Figure S5, Supporting Information) with intermediate hand grinding for the initial three-step firing, then inserting two extra milling and sintering steps to the final stages of the protocol.

The resulting protocol contains three milling and firing steps between the initial formation of MgFe_2O_4 and the final product. The PXRD patterns from each step of this protocol (Figure S7, Supporting Information) show a similar phase evolution to that of Protocol 6, however samples produced in this way appeared to be free of MgFe_2O_4 . SEM-EDX analysis and imaging of the pelletized sample confirmed its compositional homogeneity (Figure S17 and S19b, Supporting Information). The resulting $M(H)$ data showed no constriction in the 300 K $M(H)$ and a linear isotherm at 395 K (Figure S9, Supporting Information), indicating the presence of only one magnetically ordered phase at room temperature. A comparison of the thermal remanent magnetization of $x = 0.15$, $y = 0.75$ ($300 \leq T \leq 700$ K) with that of the original spinel-containing sample of $x = 0.15$, $y = 0.80$ from Protocol 0 confirms the improvement in sample purity (Figure S2a,b, Supporting Information): only a single magnetic transition is apparent which occurs at 343 K due to long-range ordering of the perovskite, where previously there were two clear transitions due to the onset of the ferrimagnetic spinel component at 586 K (Figure S2a, Supporting Information). Hence the identification of the intermediate formation of MgFe_2O_4 has allowed the development of a protocol that retained Bi_2O_3 stoichiometrically to temperatures where its reaction with the spinel allows elimination of the spinel. Dense pellets produced in this way were used for property measurements.

2.3. Physical Properties of Single-Phase (Spinel-Free) BTFM-CTO

2.3.1. Long-Range Magnetic Ordering and Intrinsic Magnetization

We will focus on data from a phase-pure sample of composition $x = 0.15$, $y = 0.75$, prepared by Protocol 7, to take advantage of magnetoelectric measurements over the entire temperature range 5–360 K. The sample was phase pure, with no spinel phase detected by laboratory PXRD data collected for 8 h (Figure 2a). Room temperature PND data show the presence of an intense magnetic Bragg reflection at 4.57 Å confirming long-range magnetic ordering in the perovskite (Figure 2b). Zero field cooled (ZFC), field cooled (FC), and thermoremanent magnetization (TRM) data confirm the onset of weak ferromagnetism at $T_N = 343$ K, which is consistent with the appearance of magnetic Bragg peaks in the high-temperature PND patterns (Figure 2d). Together with the hysteresis in the $M(H)$ data at 300 K (Figure 2c), the linear $M(H)$ isotherm at 360 K (Figure 2c) and the divergence between ZFC and FC magnetizations at T_N (Figure 2d), this demonstrates that the magnetization arises from canting of the antiferromagnetically ordered Fe^{3+} spins in the perovskite. The extracted saturated magnetization and coercive field ($\mu_0 H_c$) at 300 K are $0.0097 \mu_B/\text{Fe}$ and 0.3067 T, respectively (Figure S10, Supporting Information). The $M(H)$ loops of a spinel-containing sample of the same nominal composition are provided in Figure S11 (Supporting Information) for comparison.

2.3.2. Magnetoelectric Coupling

To probe coupling between P and M , magnetoelectric measurements were performed on a pellet poled both magnetically and

electrically. At 300 K, a linear magnetoelectric effect is observed with linear magnetoelectric susceptibility, $\alpha = 0.19$ (1) ps m^{-1} . No linear magnetoelectric effect is observed above T_N ($\alpha = 0.01$ (1) ps m^{-1} at 360 K), where the induced moment is below the instrument sensitivity limit (Figure 2e,f). This differs from the spinel-containing samples which retain a small residual linear magnetoelectric effect above T_N due to composite effects.^[18] The magnetoelectric susceptibility at 10 K is -1.51 (1) ps m^{-1} : the temperature dependence of α shows reversal of sign above 170 K and disappears near T_N . High dc resistivity ($2.33 \times 10^{12} \Omega \text{ cm}$ at 300 K), low leakage current over the entire measurement range (10 nA at 360 K) and disappearance of α at T_N (Figure 2f) ensure that the size of the intrinsic magnetoelectric coupling is well determined.

2.3.3. Ferroelectric Behavior with Large Polarization

Highly insulating behavior and low dielectric loss ($\tan \delta < 0.03$ at 100 Hz; Figure S13a, Supporting Information) allows ferroelectric measurement up to a field of 200 kV cm^{-1} . Figure 3 shows room temperature polarization–electric field hysteresis ($P(E)$) loops collected at a frequency of 10 Hz. Well saturated loops confirm ferroelectricity with maximum polarization (P_{max}) of $47.7 \mu\text{C cm}^{-2}$ at a measurement field of 200 kV cm^{-1} . Positive-up-negative-down (PUND) measurements confirm that the large measured polarization is intrinsic (Figure S13b, Supporting Information). It should be noted that polarization measured in $P(E)$ /PUND above the coercive field still increases with the measurement fields. This suggests that polarization, while switchable, is not saturated since the saturated polarization is independent of applied electric fields. In these switching fields, the remanent polarization is a function of pulse width and it tends to saturation at higher pulse width values (Figure S12, Supporting Information). To assess the saturated remanent polarization, PUND measurements were carried out against pulse width at a constant electric field of $E = 160 \text{ kV cm}^{-1}$. The remanent polarizations ($\pm dP/2$) tend to saturation at high pulse width with $P = 66 \mu\text{C cm}^{-2}$ at 626 ms (Figure 3b, Figure S13c, Supporting Information). The polarization value is higher than other known MPB systems such as PZT ($P_r = 35 \mu\text{C cm}^{-2}$), NBT–BTO ($P_r = 37.8\text{--}40 \mu\text{C cm}^{-2}$), KBT–NBT ($P_r = 38 \mu\text{C cm}^{-2}$), NBT–KBT–BTO ($P_r = 40 \mu\text{C cm}^{-2}$).^[34]

2.3.4. Depolarization and First-Order Phase Transition

BTFM-CTO ($y = 0.25$) and certain Pb-free piezoelectrics show loss of polarization at a depolarization temperature (T_d) which appears below the Curie temperature (T_{CE}).^[35,36] At room temperature, the composition $x = 0.15$, $y = 0.75$ shows a longitudinal piezoelectric coefficient (d_{33}) of 36.3 pC N^{-1} . The temperature dependence of d_{33} measured ex situ on $x = 0.15$, $y = 0.75$ shows a sharp decrease which coincides with the sharp and frequency independent peaks in the permittivity data at $T_d = 690$ K confirming a depolarization transition (Figure 4a,b). On cooling, the transition in the permittivity data appears at a lower temperature of 650 K. The sharp transition along with the thermal hysteresis in the permittivity and the heat flow data indicate a

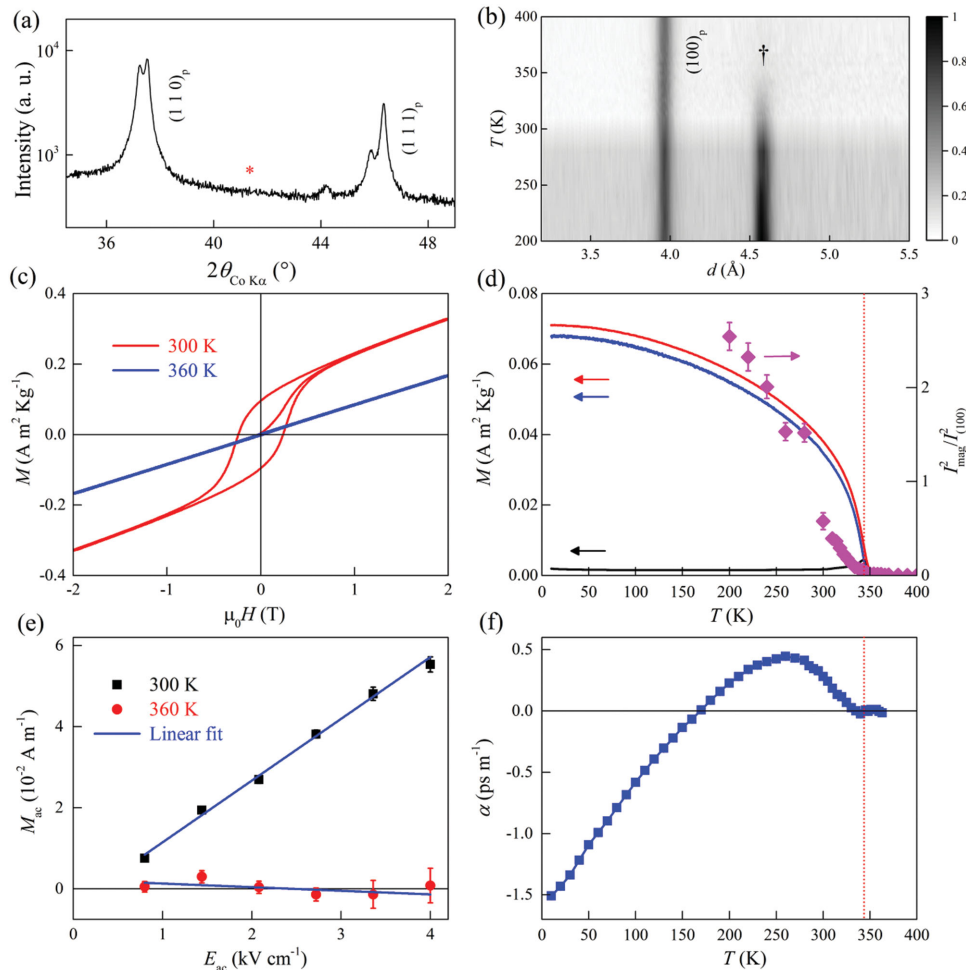


Figure 2. Diffraction, magnetic, and magnetoelectric properties of single-phase $0.85\text{BiTi}_{0.125}\text{Fe}_{0.75}\text{Mg}_{0.125}\text{O}_3-0.15\text{CaTiO}_3$ ($x = 0.15$, $y = 0.75$). a) Selected portion of laboratory PXR pattern, collected for 8 h with intensity plotted on a logarithmic scale, which does not contain a spinel peak (expected position marked by asterisk). b) PND patterns from GEM (bank 3, $2\theta = 35^\circ$) showing temperature dependence of the $(100)_p$ nuclear reflection and the main magnetic reflection (\dagger) in the temperature range 200–400 K. c) Magnetic isotherms at 300 K (red, $<T_N$) and 360 K (blue, $>T_N$) confirming the presence of a single magnetic phase. d) ZFC (black line), FC (red line) magnetization, and TRM (blue line) data (left axis) plotted with the squared ratio of magnetic Bragg peak intensity to $(100)_p$ nuclear Bragg peak intensity ($I_{\text{mag}}^2/I_{(100)}^2$) obtained from peak fitting to PND patterns (right axis, filled purple diamonds), showing that the onset of magnetization occurs simultaneously with the onset of long-range magnetic order in the perovskite. The red dotted line shows $T = T_N$. Error bars represent one standard deviation. e) Linear magnetoelectric effect at 300 K (black squares) and 360 K (red circles). The blue line shows the linear fit to the experimental data (filled symbols) and error bars represent standard errors. f) Temperature dependence of the linear magnetoelectric coefficient (α) (blue squares); error bars represent standard errors. The dotted red line shows $T = T_N$.

first-order phase transition at T_d (Figure 4b,c). The non-zero d_{33} above T_d ($d_{33} = 2.1$ and 0.1 pC N^{-1} at 773 and 1173 K, respectively) and absence of any signature of phase transition in differential scanning calorimetry (DSC) measurements up to 1173 K indicates that the Curie temperature is above 1173 K. The T_d is significantly higher than Pb-free MPB systems such as NBT-KBT ($T_d = 403\text{--}443 \text{ K}$), NBT-BTO ($T_d = 363\text{--}378 \text{ K}$), NBT-KBT-BTO ($T_d = 435 \text{ K}$) and comparable to PZT ($T_d = 659 \text{ K}$)^[37] and pseudocubic BFO-BTO ($T_d = 703 \text{ K}$)^[34,35]. Despite the low d_{33} , this high T_d is significant in a Pb-free MPB system^[35] for high-temperature piezoelectric applications.

The precise temperature of the phase transition on warming is dependent on the thermal history of the sample (Figure S14, Supporting Information), which is indicative of complex strain effects. Thermal cycling at the slow rate of 2 K min^{-1} removes

this effect to produce samples with a consistent and reproducible phase transition temperature of 690 K on warming (Figure S14, Supporting Information). The structural behavior at the depolarization temperature was then investigated by variable temperature PXR (I11) of a thermally cycled sample with 107 diffraction patterns collected on warming and cooling in the range 323–873 K. Sequential Le Bail fits using the room temperature (P11a) unit cell produced good fits up to 690 K from data collected on warming, and up to 610 K from data collected on cooling, but produced very poor fits to patterns collected above these temperatures, indicative of a structural phase transition. This is illustrated by sharp increases in the plots of normalized R_{wp} versus temperature (Figure 4d), which show transition temperatures that are consistent with the hysteresis observed in the dielectric permittivity and calorimetry

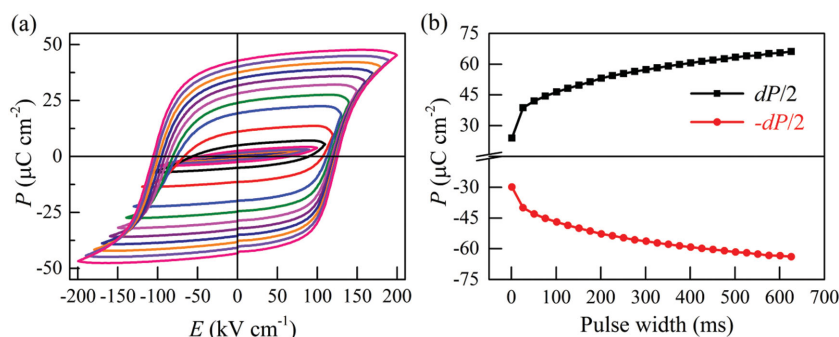


Figure 3. Ferroelectric behavior of phase-pure $0.85\text{BiTi}_{0.125}\text{Fe}_{0.75}\text{Mg}_{0.125}\text{O}_3-0.15\text{CaTiO}_3$ ($x = 0.15$, $y = 0.75$). a) $P(E)$ hysteresis loops at increasing electric fields collected at 10 Hz. b) Remanent polarization against pulse width from PUND measurements at an electric field of 160 kV cm^{-1} and a pulse delay of 1000 ms.

(Figure 4b,c), indicating that the depolarization and structural transition occur together within the resolution limit of the measurements. The structural phase transition is confirmed by inspection of the diffraction patterns, which show a discontinuous change at 690 K on warming with the appearance of several new peaks that cannot be indexed to the room temperature cell; this pattern is then retained until the sample is cooled below 610 K (Figure S15, Supporting Information). The thermal evolution of the lattice parameters on warming to the phase transition temperature are presented in Figure S16 (Supporting Information).

3. Conclusion

The identification of the spinel MgFe_2O_4 as a ferrimagnetic impurity phase in the magnetoelectric multiferroic perovskite oxide BTfM-CTO has allowed the development of a new synthetic protocol to produce single-phase samples by optimizing reaction precursors, mixing, grinding, and heating protocols systematically. Suppression of Bi_2O_3 volatilization coupled to repeated milling and sintering eliminated the refractory reaction intermediate MgFe_2O_4 ; the use of an optimal reactive Mg source and ultrapure reagents is also essential for minimizing the amount of MgFe_2O_4 formed initially. Physical characterization of the resulting phase-pure samples allowed quantitative determination of the intrinsic magnetic, magnetoelectric, and ferroelectric properties at room temperature; the composition $x = 0.15$, $y = 0.75$ has a saturated magnetization of $0.0097\mu_B$ per Fe, magnetoelectric susceptibility of $0.19\text{ (1) ps m}^{-1}$, and a polarization of $66\text{ }\mu\text{C cm}^{-2}$. PND was used to demonstrate that BTfM-CTO exhibits weak ferromagnetism and magnetoelectric coupling only when the perovskite is ordered magnetically; this can be far above room temperature in this system ($T_N = 367\text{ K}$ for the composition $x = 0.15$, $y = 0.80$). The phase-pure composition $x = 0.15$, $y = 0.75$ was shown to be ferroelectric up to a depolarization temperature of 690 K where it undergoes a structural phase transition. BTfM-CTO combines high-temperature ferroelectricity with intrinsic weak ferromagnetism and magnetoelectric coupling far above room temperature.

4. Experimental Section

Sample Preparation Protocols: Comprehensive details of synthesis protocols 0–6 are presented in the Supporting Information; only Protocol 7 (synthesis of single-phase materials) is described here. The starting materials were $(\text{MgCO}_3)_4\cdot\text{Mg}(\text{OH})_2\cdot 5\text{H}_2\text{O}$ (99.99% Sigma Aldrich), ultrapure Bi_2O_3 (99.9995% Alfa Aesar), CaCO_3 (99.997% Alfa Aesar), Fe_2O_3 (99.998% Alfa Aesar), and TiO_2 (99.995% Alfa Aesar). These were ground by hand under a small quantity of acetone. The dried reaction mixture (loose powder) was then loaded in an alumina crucible and subjected to a three-stage heating cycle of 723 K for 3 h, 923 K for 3 h, and 1023 K for 12 h with intermediate hand grinding. These temperatures were selected based on the TGA experiments on the loose powder (Figure S5, Supporting Information). The resulting powders were ball milled in ethanol for 22 h, dried, and pelletized (13 mm diameter and 1–2 mm thickness), then calcined at 1053 K for 12 h in a closed alumina crucible lined with Pt foil without any sacrificial powder. The resulting pellets were pulverized and ball milled in ethanol for 22 h, the dried powder was then pelletized (8 mm diameter and $\approx 0.5\text{ mm}$ thickness) and packed under sacrificial powder in a Pt-lined alumina boat and calcined at 1203 K for 12 h under an oxygen flow. The pellets were ground and further milled in ethanol for 22 h with 2 weight percent organic binder polyvinyl butyral (Butvar B-98) and 0.2 weight percent MnO_2 (Sigma Aldrich, 99.99%). Dried powders were pressed into pellets (diameter 8 mm, thickness $\approx 0.5\text{ mm}$), pressed isostatically to 200 MPa using a cold isostatic press, packed under sacrificial powder in Pt lined alumina boats and sintered at 1203 K for 12 h under flowing O_2 . The heating and cooling rates were 5 K min^{-1} .

During the sintering process, cracks were observed in pellets which could be reduced by decreasing sintering temperature and cooling rate. Spinel-free material was obtained in the sintering temperature range 1173–1203 K. The final sintering step carried out without sacrificial powder also resulted in spinel-free material. Ferroelectric and magnetoelectric measurements were carried out on samples whose final sintering was conducted without sacrificial powder. Density measured using Archimedes balance confirmed 93% of crystallographic density. The samples were prepared at a scale of 3 g. Pellets were cut into suitable sizes for physical property measurements. As-sintered samples were thermally cycled at 2 K min^{-1} prior to DSC, d_{33} , and PXRD measurements.

Diffraction Experiments: Routine PXRD characterization was carried out using a PANalytical X'Pert Pro diffractometer in Bragg-Brentano geometry with a monochromated $\text{Co K}\alpha_1$ source and position sensitive X'Celerator detector. Variable temperature PXRD experiments were carried out using the I11 diffractometer at Diamond Light Source (UK) with a position sensitive detector for rapid data collection and an incident wavelength of $0.825959(1)\text{ }\text{\AA}$. The sample was contained in a spinning quartz capillary of diameter 0.1 mm. The sample was scanned through temperatures of 323–873–423 K at 6 K min^{-1} in steps of 10 K, with data collected for 90 s at each temperature. Le Bail fits were carried out using Topas Academic (version 5). Variable temperature time-of-flight neutron powder diffraction patterns were collected using the Polaris (compositions $x = 0.15$, $y = 0.60$ and $x = 0.15$, $y = 0.80$) and GEM (composition $x = 0.15$, $y = 0.75$) diffractometers at ISIS Spallation Source (UK). Samples were contained in thin walled vanadium cans. The raw intensities of the (100) nuclear peak (I_{100}) and the magnetic peak (I_{mag}) were extracted by peak fitting in Topas Academic (version 5). The two peaks were fitted simultaneously using a refined pseudo-Voigt peak shape with a refined Chebyshev background function. The peak shape was constrained to be identical for the two peaks.

Ferroelectric Measurements: Pellets were cut to suitable size ($2\text{--}5\text{ mm}^2$) and polished down to 100–160 μm with tolerance of 10 μm using a Tegramin 30 (Struers) semi-automatic polishing machine. Silver

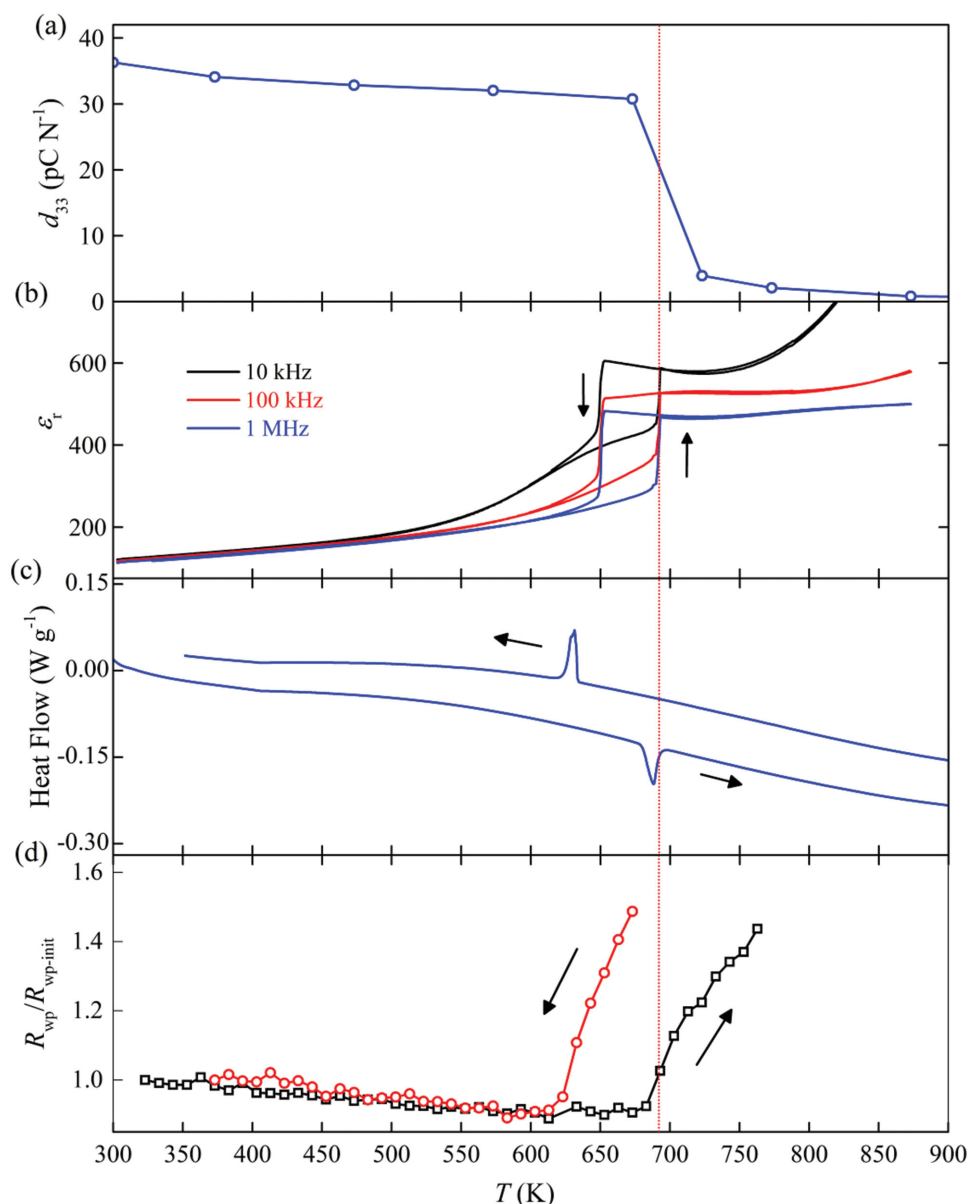


Figure 4. Depolarization in $0.85\text{BiTi}_{0.125}\text{Fe}_{0.75}\text{Mg}_{0.125}\text{O}_3-0.15\text{CaTiO}_3$ ($x = 0.15$, $y = 0.75$). Temperature dependence of a) d_{33} measured ex situ, b) dielectric permittivity (ϵ_r), c) heat flow, and d) normalized R_{wp} values from Le Bail fits to variable temperature synchrotron XRD data using a single-phase monoclinic structural model (space group $P11a$); together confirming the first-order structural transition at the depolarization temperature T_d , shown by a red dotted line. Arrows indicate measurements on heating and cooling.

paint was applied on both sides of the pellet; any silver within $\approx 20 \mu\text{m}$ of the edges was then removed using acetone-wet cotton buds to minimize the likelihood of dielectric breakdown. The pellet was immersed in silicone oil in a Radiant high voltage test fixture. P(E) and positive-up-negative-down (PUND) measurements were carried out using a Radiant Precision LC ferroelectric tester.

To assess the remanent part of the measured polarization, PUND measurements were carried out. A typical PUND profile (Figure S13, Supporting Information) confirms that the non-remnant part (P^*) is much smaller compared to the total polarization (P^*) which contains both remanent and non-remnant parts. The remanent polarizations are calculated as $+dP/2 = (P^* - P^*)/2$ and $-dP/2 = (-P^* - (-P^*))/2$. In the intermediate state, where the polarization is switchable but not completely saturated, the remanent polarizations are a function of

the pulse width as shown for a commercial PZT ceramic PIC151 (Figure S12a,b, Supporting Information).

d_{33} Measurements: For d_{33} measurements, silver paint was applied on both sides of a polished pellet. To carry out poling, the pellet was immersed in silicone oil in the high-temperature sample holder of the aixPES equipment (aixACCT Systems GmbH). An electric field of 100 kV cm^{-1} was applied at 373 K for 15 min . The sample was then cooled down at 1 K min^{-1} to room temperature and the voltage was switched off. The piezoelectric charge coefficient d_{33} was measured after 24 h in a piezometer PM300 (Piezotest Pte Ltd) using a sinusoidal force of 0.25 N at 110 Hz . For depolarization measurements, the poled pellet was shorted using a Pt wire clip and depoled at a particular temperature for 1 h in a temperature controlled furnace. The d_{33} was then measured using the piezometer after depoling ex situ.

Received: November 16, 2015
Revised: December 21, 2015
Published online: February 5, 2016

DSC and TGA Measurements: Heat flow was measured using DSC option in a SDT Q600 (TA Instruments). TGA experiments were performed using a Q500 thermogravimetric analyzer (TA instruments). The sample was placed in a Pt pan under flowing air (10–20 mL min⁻¹). The heating and cooling rates were 2–10 K min⁻¹.

Dielectric Measurements: For dielectric measurements a Pt paste was applied on both sides of a pellet and cured at 1123 K for 30 min. Capacitance (C) and loss (tanδ) were measured using an Agilent LCR meter E4980 by applying an AC voltage of 0.2 V in the frequency range 1 kHz to 1 MHz. The sample was loaded in a custom made sample holder and data were collected using the LABVIEW software program. A ramp rate of 2 K min⁻¹ was used.

Magnetic Measurements: Magnetic measurements were carried out using the vibrating sample magnetometer option of the MPMS3 system (Quantum Design, USA). Pellet samples were fixed to a quartz sample holder and then loaded into a SQUID probe. Temperature dependence of magnetization was measured in ZFC, FC, and TRM modes. For measurements in the 10–395 K range, the sample is cooled down to 10 K under zero applied field and magnetic field of $\mu_0 H = 0.01$ Tesla is applied. The moment is measured (i) while warming up (ZFC) to 395 K, (ii) while cooling down from 395 to 10 K under the same applied field (FC). The field is set to zero at 10 K and the moment is measured while warming up (TRM). A ramp rate of 3 K min⁻¹ was used. Magnetic measurements in the temperature range 300–700 K were carried out using the oven option in the MPMS3 system. The Néel temperature (T_N) is derived from peak in the derivative of TRM data. The saturated magnetization was obtained by subtracting the linear contribution from M(H) isotherms as described in previous studies.^[18,38]

Magnetoelectric Measurements: Linear magnetoelectric measurements were performed with a custom setup using a SQUID magnetometer MPMS XL7 (Quantum Design, USA). Details and measurement protocol are described in previous works.^[18,38] Prior to magnetoelectric measurements, pellets were poled externally using aixPES (as described in reference^[18]) and then subjected to a magnetic field ($\mu_0 H$) of 2 T for 60 min. After removal of fields, electrodes were short circuited for 15 min prior to conducting magnetoelectric measurements. The leakage current is low in the entire measurement range (10 nA at 360 K at 4 kV cm⁻¹ for spinel-free composition $x = 0.15$, $y = 0.75$).

Scanning Electron Microscopy and Energy Dispersive X-Ray Spectroscopy: Scanning electron microscopy (SEM) was performed with an FE-SEM Hitachi S-4800 equipped with an Oxford Instruments EDX detector. Samples, in powder or pellet form, were attached to a carbon tape stuck on an aluminum stub. In order to minimize the charging effect, a thin layer of gold (2–3 nm) was sputtered on the samples surface. Energy dispersive X-ray spectroscopy (EDX) data were collected in at least nine different areas for each sample. The quantification data, for each element, were corrected using a correction factor determined using a standard.

Supporting Information

Supporting Information is available from the Wiley Online Library or from the author.

Acknowledgements

This work was supported by EPSRC under EP/H000925/1. Synchrotron X-ray diffraction was carried out with the support of Diamond Light Source (UK). Time-of-flight neutron diffraction experiments were carried out with the support of ISIS Spallation Source (UK). We thank Dr. C. Tang, Dr. C. Murray, and Dr. S. Day for assistance on beamline I11 (DLS), Dr. R. I. Smith for assistance on Polaris (ISIS), and Dr. I. da Silva for assistance on GEM (ISIS). M.J.R. is a Royal Society Research Professor.

- [1] W. Eerenstein, N. D. Mathur, J. F. Scott, *Nature* **2006**, 442, 759.
- [2] M. Fiebig, *J. Phys. D: Appl. Phys.* **2005**, 38, R123.
- [3] J. F. Scott, *Nat. Mater.* **2007**, 6, 256.
- [4] M. Bibes, A. Barthelemy, *Nat. Mater.* **2008**, 7, 425.
- [5] G. A. Smolenski, I. E. Chupis, *Sov. Phys. Usp.* **1982**, 25, 475.
- [6] I. Sosnowska, T. P. Neumaier, E. Steichele, *J. Phys. C: Solid State Phys.* **1982**, 15, 4835.
- [7] Yu. F. Popov, A. K. Zvezdin, G. P. Vorob'ev, A. M. Kadomtseva, V. A. Murashev, D. N. Rakov, *JETP Lett.* **1993**, 57, 69.
- [8] C. Ederer, N. A. Spaldin, *Phys. Rev. B* **2005**, 71, 060401.
- [9] J. Wang, J. B. Neaton, H. Zheng, V. Nagarajan, S. B. Ogale, B. Liu, D. Viehland, V. Vaithyanathan, D. G. Schlom, U. V. Waghmare, N. A. Spaldin, K. M. Rabe, M. Wuttig, R. Ramesh, *Science* **2003**, 299, 1719.
- [10] J. T. Heron, M. Trassin, K. Ashraf, M. Gajek, Q. He, S. Y. Yang, D. E. Nikonov, Y.-H. Chu, S. Salahuddin, R. Ramesh, *Phys. Rev. Lett.* **2011**, 107, 217202.
- [11] J. T. Heron, J. L. Bosse, Q. He, Y. Gao, M. Trassin, L. Ye, J. D. Clarkson, C. Wang, J. Liu, S. Salahuddin, D. C. Ralph, D. G. Schlom, J. Íñiguez, B. D. Huey, R. Ramesh, *Nature* **2014**, 516, 370.
- [12] S. A. Ivanov, S. Eriksson, N. W. Thomas, R. Tellgren, H. Rundlof, *J. Phys.: Condens. Matter* **2001**, 13, 25.
- [13] I. P. Raevski, V. V. Titov, M. A. Malitskaya, E. V. Eremin, S. P. Kubrin, A. V. Blazhevich, H. Chen, C.-C. Chou, S. I. Raevskaya, I. N. Zakharchenko, D. A. Sarychev, S. I. Shevtsova, *J. Mater. Sci.* **2014**, 49, 6459.
- [14] N. A. Lomanova, V. G. Semenov, V. V. Panchuk, V. V. Gusarov, *J. Alloys Compd.* **2012**, 528, 103.
- [15] M. Mazurek, D. Oleszak, T. Pikula, M. Karolus, E. Jartych, *Acta Phys. Pol. A* **2014**, 126, 975.
- [16] D. M. Evans, A. Schilling, A. Kumar, D. Sanchez, N. Ortega, M. Arredondo, R. S. Katiyar, J. M. Gregg, J. F. Scott, *Nat. Commun.* **2013**, 4, 1534.
- [17] L. Keeney, T. Maity, M. Schmidt, A. Amann, N. Deepak, N. Petkov, S. Roy, M. E. Pemble, R. W. Whatmore, *J. Am. Ceram. Soc.* **2013**, 96, 2339.
- [18] P. Mandal, M. J. Pitcher, J. Alaria, H. Niu, P. Borisov, P. Stamenov, J. B. Claridge, M. J. Rosseinsky, *Nature* **2015**, 525, 363.
- [19] J. Frantti, *J. Phys. Chem. B* **2008**, 112, 6521.
- [20] N. Zhang, H. Yokota, A. M. Glazer, Z. Ren, D. A. Keen, D. S. Keeble, P. A. Thomas, Z.-G. Ye, *Nat. Commun.* **2014**, 5, 5231.
- [21] S. L. Swartz, T. R. Shrout, *Mater. Res. Bull.* **1982**, 17, 1245.
- [22] S. Vijayanand, H. S. Potdar, P. A. Joy, *Appl. Phys. Lett.* **2009**, 94, 182507.
- [23] N. Jeon, D. Rout, I. W. Kim, S.-J. L. Kang, *Appl. Phys. Lett.* **2011**, 98, 072901.
- [24] C. Nayek, A. Tamilselvan, C. Thirimal, P. Murugavel, S. Balakumar, *J. Appl. Phys.* **2014**, 115, 073902.
- [25] M. Valant, A.-K. Axelsson, N. Alford, *Chem. Mater.* **2007**, 19, 5431.
- [26] M. S. Bernardo, T. Jardiell, M. Peiteado, A. C. Caballero, M. Villegas, *J. Eur. Ceram. Soc.* **2011**, 31, 3047.
- [27] T. Rojac, A. Bencan, B. Malic, G. Tutuncu, J. L. Jones, J. E. Daniels, D. Damjanovic, *J. Am. Ceram. Soc.* **2014**, 97, 1993.
- [28] S. M. Selbach, M.-A. Einarsrud, T. Grande, *Chem. Mater.* **2009**, 21, 169.
- [29] R. Köferstein, T. Buttler, S. G. Ebbinghaus, *J. Solid State Chem.* **2014**, 217, 50.

- [30] A. A. Zatsiupa, L. A. Bashkurov, I. O. Troyanchuk, G. S. Petrov, A. I. Galyas, L. S. Lobanovsky, S. V. Truhanov, *J. Solid State Chem.* **2014**, 212, 147.
- [31] N. Shamir, E. Gurewitz, H. Shaked, *Acta Crystallogr. Sect. A* **1978**, 34, 662.
- [32] Q. Chen, Z. J. Zhang, *Appl. Phys. Lett.* **1998**, 73, 3156.
- [33] R. L. White, *J. Appl. Phys.* **1969**, 40, 1061.
- [34] J. Rödel, W. Jo, K. T. P. Seifert, E.-M. Anton, T. Granzow, D. Damjanovic, *J. Am. Ceram. Soc.* **2009**, 92, 1153.
- [35] S. O. Leontsev, R. E. Eitel, *Sci. Technol. Adv. Mater.* **2010**, 11, 044302.
- [36] P. Mandal, A. Manjón-Sanz, A. J. Corkett, T. P. Comyn, K. Dawson, T. Stevenson, J. Bennett, L. F. Henrichs, A. J. Bell, E. Nishibori, M. Takata, M. Zanella, M. R. Dolgos, U. Adem, X. Wan, M. J. Pitcher, S. Romani, T. T. Tran, P. S. Halasyamani, J. B. Claridge, M. J. Rosseinsky, *Adv. Mater.* **2015**, 27, 2883.
- [37] H. Jaffe, *J. Am. Ceram. Soc.* **1958**, 41, 494.
- [38] M. J. Pitcher, P. Mandal, M. S. Dyer, J. Alaria, P. Borisov, H. Niu, J. B. Claridge, M. J. Rosseinsky, *Science* **2015**, 347, 420.
-